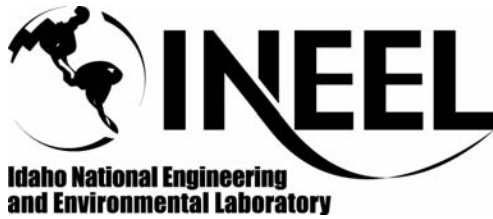# CFD Model Of A Planar Solid Oxide Electrolysis Cell For Hydrogen Production From Nuclear Energy

Grant L. Hawkes
James E. O'Brien
Carl M. Stoots
J. Stephen Herring
Mehrdad Shahnam

October 2-6, 2005

The 11th International Topical Meeting On Nuclear Reactor Thermal-Hydraulics (NURETH-11)

CFD MODEL OF A PLANAR SOLID OXIDE ELECTROLYSIS CELL FOR HYDROGEN PRODUCTION FROM NUCLEAR ENERGY

Grant L. Hawkes[1], James E. O'Brien, Carl M. Stoots, J. Stephen Herring
Idaho National Laboratory
2525 N. Fremont Ave., Idaho Falls, ID, 83415, USA
haw@inel.gov   +1 (1) 208 526 8767

Mehrdad Shahnam
FLUENT Inc.
3647 Collins Ferry Road, Suite A, Morgantown, WV, 26505, USA
ms@fluent.com   +1 (1) 304 598 3770

ABSTRACT

A three-dimensional computational fluid dynamics (CFD) model has been created to model high-temperature steam electrolysis in a planar solid oxide electrolysis cell (SOEC). The model represents a single cell as it would exist in an electrolysis stack. Details of the model geometry are specific to a stack that was fabricated by Ceramatec[2], Inc. and tested at the Idaho National Laboratory. Mass, momentum, energy, and species conservation and transport are provided via the core features of the commercial CFD code FLUENT[2]. A solid-oxide fuel cell (SOFC) model adds the electrochemical reactions and loss mechanisms and computation of the electric field throughout the cell. The FLUENT SOFC user-defined subroutine was modified for this work to allow for operation in the SOEC mode. Model results provide detailed profiles of temperature, Nernst potential, operating potential, anode-side gas composition, cathode-side gas composition, current density and hydrogen production over a range of stack operating conditions. Mean model results are shown to compare favorably with experimental results obtained from an actual ten-cell stack tested at INL.

KEYWORDS

High-temperature electrolysis, computational fluid dynamics, hydrogen production, nuclear energy.

1. INTRODUCTION

Currently there is strong interest in the large-scale production of Hydrogen as a secondary energy carrier for the non-electrical market. Hydrogen is of particular interest as the secondary energy carrier because it has the potential to be storable, transportable, and environmentally benign. Hydrogen can be used as a fuel for heating, electrical production (using fuel cells), and vehicles. It is also used as a raw material for many chemical processes, such as ammonia and methanol synthesis, iron ore processing, petroleum processing, and others. Hydrogen is now produced primarily via steam reforming of methane. From a long-term perspective, methane reforming is not a viable process for large-scale production of hydrogen as a major energy carrier since such fossil fuel conversion processes consume non-renewable resources and emit greenhouse gases to the environment.

---

[1] Corresponding author

[2] References herein to any specific commercial product, process, or service by trade name, trademark, manufacturer, or otherwise, does not necessarily constitute or imply its endorsement, recommendation, or favoring by the U.S. Government, any agency thereof, or any company affiliated with the Idaho National Laboratory

Consequently, there is a high level of interest in production of hydrogen from water splitting via either thermochemical or electrolytic processes (e.g., National Research Council, 2004).

High-temperature nuclear reactors have the potential for substantially increasing the efficiency of hydrogen production from water splitting, with no consumption of fossil fuels, no production of greenhouse gases, and no other forms of air pollution. Thermal water-splitting for hydrogen production can be accomplished via high-temperature electrolysis or thermo-chemical processes, using high-temperature nuclear process heat. In

Figure 1. Detail of SOEC stack.

order to achieve competitive efficiencies, both processes require high-temperature operation (~850°C). Thus these hydrogen-production technologies are tied to the development of advanced high-temperature nuclear reactors. High-temperature electrolytic water splitting supported by nuclear process heat and electricity has the potential to produce hydrogen with overall system efficiency near those of the thermochemical processes (Yildiz, 2003; IAEA, 1999), but without the corrosive conditions of thermochemical processes and without the fossil fuel consumption and greenhouse gas emissions associated with hydrocarbon processes. Specifically, a high-temperature advanced nuclear reactor coupled with a high-efficiency high-temperature electrolyzer could achieve a competitive thermal-to-hydrogen conversion efficiency of 45 to 55%.

A research program is under way at the Idaho National Laboratory (INL) to simultaneously address the research and scale-up issues associated with the implementation of planar solid-oxide electrolysis cell technology for hydrogen production from steam. The research program includes an experimental program aimed at performance characterization of electrolysis cells and stacks. Results of some of the single-cell tests have been documented in several recent papers (O'Brien et al., Herring et al., 2004). Single (button) cell tests are useful for basic performance characterization of electrode and electrolyte materials and of different cell designs (e.g., electrode-supported). The single-cell results demonstrated efficient small-scale hydrogen production, with performance close to theoretical predictions. Cell performance was shown to be continuous from the fuel-cell to the electrolysis mode. The effects of steam starvation and thermal cycling on cell performance parameters were discussed. Based on these preliminary results, high-temperature electrolysis appears to be a viable means for hydrogen production using nuclear energy.

The INL research program also includes modeling and materials development tasks. For detailed SOEC modeling, the commercial CFD code FLUENT was selected. Fluent Inc. was funded by the US Department of Energy National Energy Technology Laboratory (DOE-NETL) to develop a solid-oxide fuel cell (SOFC) module for coupling to the core mass, momentum, energy, and species conservation and transport features of the FLUENT CFD code (Prinkey et al., 2004). The SOFC module adds the electrochemical reactions and loss mechanisms and computation of the electric field throughout the cell. The FLUENT SOFC user-defined subroutine was modified for this work to allow for operation in the SOEC mode. Model results provide detailed profiles of temperature, Nernst potential, operating potential, anode-side gas composition, cathode-side gas composition, current density and hydrogen production over a range of stack operating conditions. Results of the numerical model are compared to experimental results obtained from a ten-cell stack tested at INL.
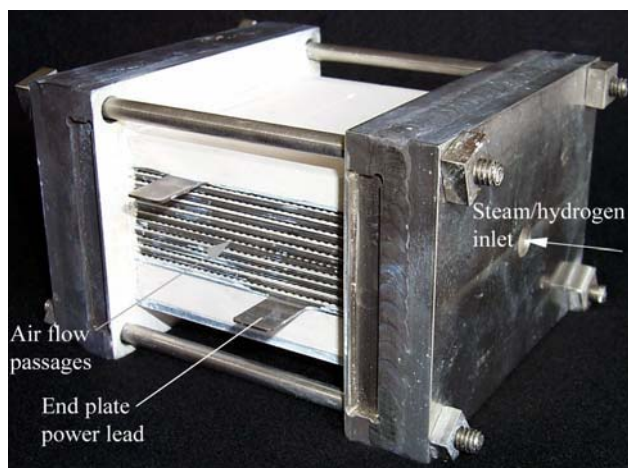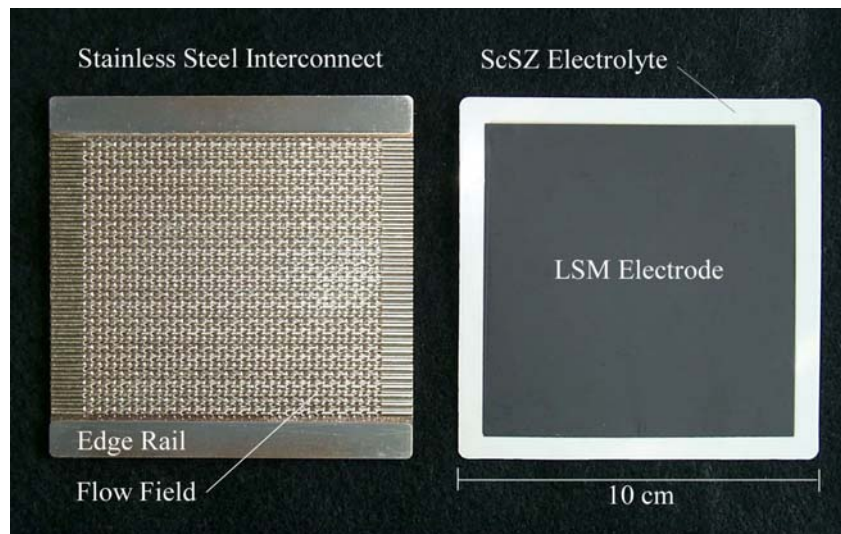
Figure 2. Interconnect plate and single electrolysis cell.

2.   NUMERICAL MODEL

The numerical model developed for this paper was based on the geometry of a single SOEC cell taken from a stack designed and fabricated by Ceramatec, Inc. and tested at the INL. A photograph of this stack is shown in Figure 1. The stack has a per-cell active area of 64 cm^2. It is designed to operate in cross flow, with the steam/hydrogen gas mixture entering the inlet manifold on the right in the photograph, and exiting through the outlet manifold, visible on the left in the photograph. Air flow enters at the rear though an air inlet manifold (not visible in Fig. 1) and exits at the front directly into the furnace. The power lead attachment tabs, integral with the upper and lower interconnect plates are also visible in the photograph.

The internal components of the stack are shown in Figure 2. The interconnect plate, shown on the left in Figure 2, is fabricated primarily from low-chromium ferritic stainless steel. It includes an impermeable separator plate (~0.46 mm thick) with edge rails and two corrugated/perforated "flow fields," one on the air side and one on the steam/hydrogen side, arranged in cross flow. The height of the flow channel formed by the edge rails and flow fields is 1.02 mm. Each flow field includes 32 perforated flow channels across its width to provide uniform gas-flow distribution. The steam/ hydrogen flow field is fabricated from nickel. The air-side flow field is ferritic stainless steel. The interconnect plates and flow fields also serve as electrical conductors and current distributors.

The electrolyte/electrode assembly is shown on the right of Figure 2. The electrolyte is scandia-stabilized zirconia, about 140 μm thick. The air-side electrode (anode in the electrolysis mode), visible in the figure, is strontium-doped lanthanum manganite (LSM). The electrode is graded, with an inner cathode layer of LSM/zirconia (~13 μm) immediately adjacent to the electrolyte and an outer cathode layer of pure LSM (~18 μm). The steam/hydrogen electrode (cathode in the electrolysis mode) is also graded, with a nickel-zirconia cermet layer (~13 μm) immediately adjacent to the electrolyte and a pure Nickel outer layer (~10 μm).

The numerical model geometry represents a single cell, as it would exist in the stack. The numerical domain extends from the center plane of one separator plate to the center plane of the next separator plate. Symmetry boundaries are applied at the top and bottom of the model. Representations of the numerical model are presented in Figure 3. In the top left portion of Figure 3, the full model is shown to scale. Since the model includes only one cell, the model geometry is quite thin in the vertical (z) direction. To show more detail, the model is shown in the bottom left portion of Figure 3 with a vertical exaggeration of 10x in the z-direction. An exploded view with the 10x vertical exaggeration is shown in the right half of the figure.
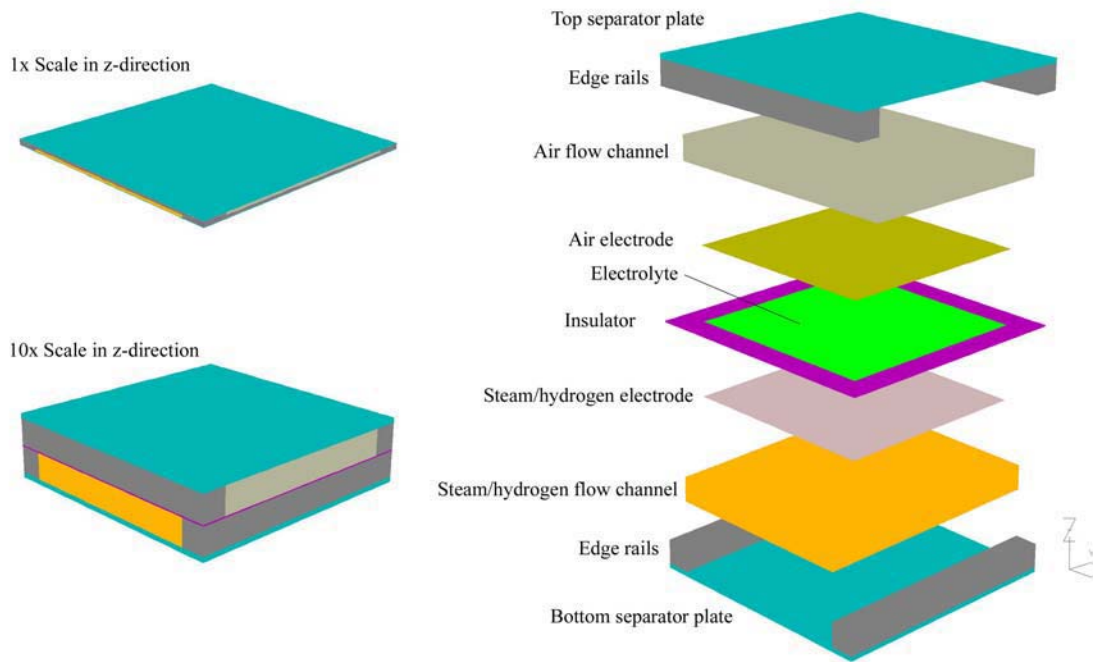
Figure 3. Fluent single-cell SOEC model.

In the exploded view, the bottom element is the bottom separator plate. Since we are trying to represent a unit cell extracted from a larger stack, the bottom and top separator plates in the numerical model are only half as thick (i.e., 0.19 mm) as the hardware separator plates. Therefore, the top and bottom boundaries of the numerical model represent symmetry planes and the boundary conditions on those faces are set accordingly. The edge rails are shown attached to the bottom separator plate. In the stack hardware, the edge rails are fabricated from the same material as the separator plates, but they are separate pieces. This is why we have used a separate color to represent the edge rails. Properties of the separator plates and edge rails (ferritic stainless) used in the model include thermal conductivity k = 27.0 W/m K, and electrical conductivity, $\sigma = 8.50 \times 10^5 \ \Omega^{-1} m^{-1}$.

The next element in the numerical model is the steam/hydrogen flow channel. The flow channels are the regions in the stack between the separator plate, the edge rails and the electrodes in which the corrugated/perforated "flow fields" are located. The steam/hydrogen flow channel has been specified as a high-porosity ($\varphi = 0.87$) porous media region with metallic nickel as the solid material and with anisotropic permeability, much higher in the primary flow direction ($K = 2 \times 10^{-4} \ m^2$) than in the cross flow directions ($K = 2 \times 10^{-5} \ m^2$). The thermal and electrical conductivities of the nickel metal were specified at 800ºC (k = 72.0 W/m K, $\sigma = 2.20 \times 10^6 \ \Omega^{-1} m^{-1}$). The height of the flow channel is the set by the thickness of the edge rails, 1.019 mm.

The next three layers in the numerical model are associated with the electrolyte/electrode assembly, as shown in the right half of Figure 2. The steam/hydrogen electrode is modeled as an isotropic porous media, nickel zirconia cermet with 25 µm thickness, $K = 10^{-13} \ m^2$, $\varepsilon = 0.37$, tortuosity $L_t = 3.0$, thermal conductivity $k = 13.1$ W/m-K, and electrical conductivity $\sigma = 1.129 \times 10^5 \ \Omega^{-1} m^{-1}$. The electrolyte is modeled as a dense impermeable layer of yttria-stabilized zirconia (YSZ), thickness 140 µm, k = 2.16 W/ m K, with a temperature-dependent ionic resistivity, $\rho(T) = 3.685 \times 10^{-4} + 2.838 \times 10^{-5} \exp(10300/T(K))$. The air electrode is modeled as an isotropic porous media, lanthanum strontium manganite (LSM) with 25 µm thickness, $K = 10^{-13} \ m^2$, $\varphi = 0.37$, tortuosity $L_t = 3.0$, thermal conductivity $k = 9.6$ W/m K, and electrical conductivity $\sigma = 7.045 \times 10^3 \ \Omega^{-1} m^{-1}$.

The FLUENT SOFC module treats the electrolyte as a 2-D planar element. Therefore the electrolyte in the model has geometrical thickness of zero. On either side of the electrolyte are the electrodes that are created with 3-D elements. Therefore, the electrolyte/electrode assembly in the model is only as thick as the two electrodes. Around the outer periphery of the electrolyte/electrode
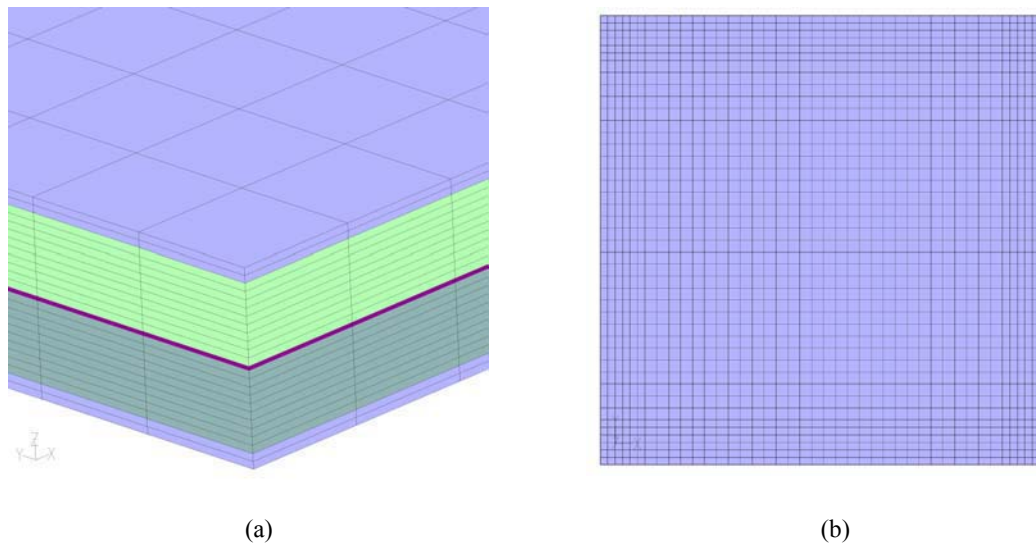
(a)   (b)

Figure 4. Details of 3D numerical mesh; (a) closeup of corner, showing vertical element stacking, (b) top view, showing 42 x 42 element grid.

assembly, we have included an "insulator" with the properties of YSZ. The insulator prevents an electrical short circuit between the top and bottom edge rails. No ionic transport occurs through this insulator.

The next element in the numerical model is the air/oxygen flow channel. It has also been specified as a high-porosity ($\varphi = 0.87$) porous media region with ferritic stainless steel as the solid material and with the same anisotropic permeabilities and flow channel height used in the steam/hydrogen flow channel. The top separator plate and edge rails are identical to those on the bottom, but the edge rails are oriented perpendicular to the bottom edge rails to allow for the cross flow arrangement. The bottom separator plate in the FLUENT model serves as the electrical ground and the top separator plate serves as the current source.

The numerical grid used in this study included 42 elements in the X and Y directions and 28 elements through the thickness, for a total of 49392 elements and 59136 nodes. Two views of the numerical grid used in the FLUENT model are shown in Figure 4. Figure 4(a) is a corner view showing 28 elements stacked in the z-direction, representing 6 distinct layers. Figure 4(b) is a top view showing the 42 x 42 element grid pattern used in the model. The top layer of two elements in Figure 4(a) is the top separator plate (half thickness). The next layer of 10 elements is the edge rail/air flow channel region. The center magenta layers visible in Figure 4(a) represent the insulator/electrode regions. There are 2 elements for each insulator/electrode layer. The next layer of 10 elements in Figure 4(a) is the edge rail/steam-hydrogen flow channel region. The bottom layer of 2 elements is the bottom separator plate (half-thickness). Note that since the FLUENT SOFC module treats the electrolyte as a 2-D planar element, the electrolyte is not visible in Figure 4(a).

Two grid sensitivity studies were performed. In the first study, the grid resolution was doubled in all three coordinate directions, resulting in a factor of 8 increase in the total number of elements. Results of this study indicated agreement to four significant digits in predicted temperatures, voltages, species compositions, etc. The second grid sensitivity was performed to address concerns about the aspect ratio of the cells used in the numerical grid. Many of the cells do have high aspect ratio (i.e. much larger dimensions in the X and Y directions compared to the Z direction) because of the thinness of the actual geometrical layers that make up the planar electrolysis cells. In order to address this concern, a second grid sensitivity study was performed in which the grid resolution was doubled in
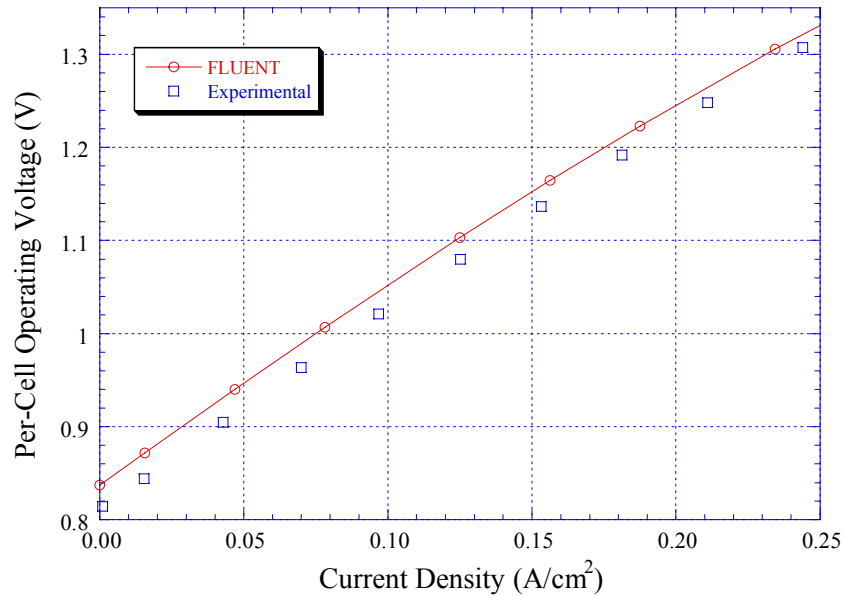
Figure 5. Voltage-current characteristics of actual electrolysis stack and FLUENT model.

both the X and Y directions, but not in the Z-direction. This refinement also shows agreement to four significant digits in temperatures, voltages and species compositions.

Additional parameters specified in the numerical model include the electrode exchange current densities and several gap electrical contact resistances. These quantities were determined empirically by comparing FLUENT predictions with stack performance data. Referring to the voltage-current density curve shown in Figure 5, the slope of the FLUENT curve is determined primarily by the values used for the gap resistances. The curvature of the Vi curve is determined by the values used for the exchange current densities. The measured stack open-cell potential for this particular test was low compared to theoretical, probably due to some preferential leakage of hydrogen due to diffusion through the porous ceramic paste that is used to seal the cells. The FLUENT V-i curve predicts the correct open-cell voltage (OCV). The authors felt that it was most important to reproduce the correct slope of the V-i curve, and not worry about the offset too much since we think we know what the reason is. The FLUENT model uses the electrode exchange current densities to quantify the magnitude of the activation overpotentials via a Butler-Volmer equation [Prinkey et al., 2004]. Higher values of exchange current density indicate lower activation overpotentials. Generally the activation overpotential associated with the steam/hydrogen electrode (the anode in fuel-cell mode) is negligible, so a very large value of exchange current density was used for this electrode. The activation overpotential for the air/oxygen electrode can be significant, especially for low-temperature fuel cells. However, based on the linearity of DC potential sweep data obtained from button cells (O'Brien et al, 2004) operated over a voltage range from the fuel-cell mode to the electrolysis mode, through the zero-current-density point, there was no indication of any significant activation overpotential for these solid-oxide cells at temperatures of 800ºC or higher. Accordingly, a relatively large value of exchange current density was used for the air/oxygen electrode as well. A relatively thick electrolyte has masked the activation overpotential. The comparison presented in Figure 5 shows the predicted V-i values using gap resistance values of 0.5 Ω cm^2 at the interfaces between the flow fields and the electrodes, and an exchange current density value of 4000 A/cm^2 at the air/oxygen electrode. An exchange current density value of 10^{20} was used on the steam/hydrogen electrode.

    A radiation heat transfer boundary condition was applied around the periphery of the model to simulate the thermal conditions of our experimental stack, situated in a high-temperature electrically heated radiant furnace. The edges of the numerical model are treated as a small surface in a large enclosure with an effective emissivity of 1.0, subjected to a radiant temperature of 1103 K, equal to the gas-inlet temperatures.

The gas flow inlets are specified in the FLUENT model as mass-flow inlets, with the gas inlet temperatures are set at 1103 K and the inlet gas composition determined by specification of the mass fraction of each component. The gas flow rates used in the model were the same as those used for the experimental base case, on a per-cell basis. For example, the base case for the steam/hydrogen inlet used a total inlet mass flow rate of 8.053×10^{-6} kg/s, with nitrogen, hydrogen and steam mass fractions of 0.51, 0.0074, and 0.483, respectively. The base case air flow rate was 4.33×10^{-6} kg/s.

Details of the core mass, momentum, energy, and species conservation and transport features of FLUENT are documented in detail in the FLUENT user manual (FLUENT, 2004). Details of the electrochemical reactions, loss mechanisms, electric field computation, and electrode porous media constitutive relations are documented by Prinkey et al. (2004). This reference also documents the treatment of species and energy sources and sinks arising from the electrochemistry at the electrode-electrolyte interfaces.

3.   DISCUSSION

There are several important fundamental differences between the fuel-cell and electrolysis modes of operation. From the standpoint of heat transfer, operation in the fuel-cell mode typically necessitates the use of significant excess air flow in order to prevent overheating of the stack. The potential for overheating arises from two sources: (1) the hydrogen oxidation reaction is exothermic, and (2) the electrolyte ionic resistance and any other resistances such as electrode resistance, contact resistance, etc., produce ohmic heating. In the electrolysis mode, the steam reduction reaction is endothermic. Therefore, depending on the operating voltage, the net heat generation in the stack may be negative, zero, or positive. This phenomenon is illustrated in Figure 6. The figure shows the respective heat fluxes in a planar solid-oxide stack associated with the electrochemical reaction and the ohmic heating. The net heat flux is also shown. A stack-average per-cell area-specific resistance of 1.25 Ω-cm^2, an operating temperature of 1200 K, and hydrogen mole fractions of 0.1 and 0.95 at the inlet and outlet, respectively, were assumed for these calculations. In the fuel-cell mode, the net heat flux is always positive and increases rapidly with current density. In the electrolysis mode, the net heat flux is negative at low current densities, increasing to zero at the "thermal-neutral" voltage, and positive at higher current densities. Assuming the process occurs at a specified temperature, the thermal-neutral voltage can be predicted from direct application of the First Law to the overall system:
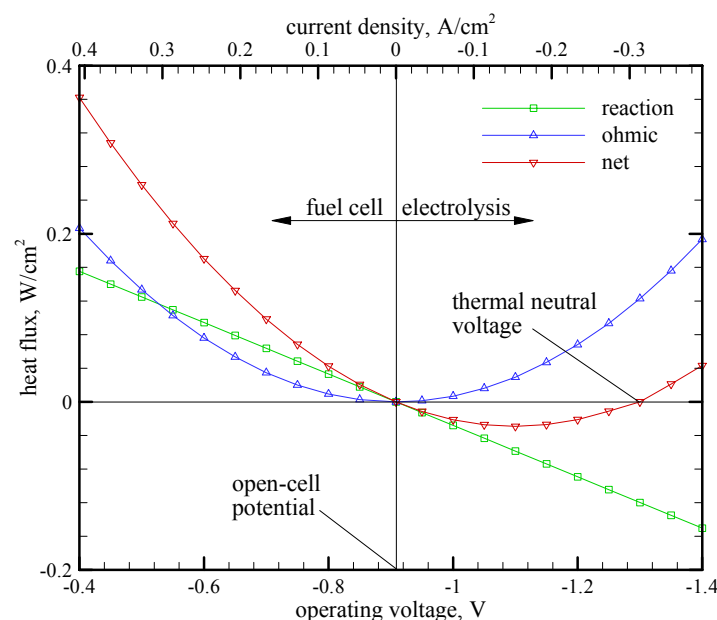

Figure 6. Thermal contributions in electrolysis and fuel cell modes of operation.

$$Q - W = \dot{N}_{H2}\Delta H_R \tag{1}$$

Letting $Q = 0$ (no external heat transfer), $W=VI$, and noting that the electrical current is directly related to the molar production rate of hydrogen by

$$\dot{N}_{H2} = I/2F \tag{2}$$

where F is the Faraday number (F = 96,487 J/V mol), yields:

$$V_{tn} = -\Delta H_R/2F \tag{3}$$

Since the molar enthalpy of reaction, ΔH_R, is strictly a function of temperature (albeit a very weak function), the thermal-neutral voltage is also strictly a function of temperature, independent of cell ASR and gas compositions. The particular values of net cell heat flux at other operating voltages do however depend on cell ASR and gas compositions. The thermal-neutral voltage increases only slightly in magnitude over the typical operating temperature range for steam electrolysis cells, from 1.287 V at 800°C to 1.292 V at 1000°C. Stack operation at or below the thermal-neutral voltage simplifies thermal management of the stack since excess air flow is not required. In fact, in the electrolysis mode, since oxygen is being produced, there is also no theoretical need for air flow to support the reaction at all. In a large-scale electrolysis plant, the pure oxygen produced by the process could be saved as a valuable commodity. Careful consideration must be given, however, to the choice of materials for containing pure oxygen at elevated temperatures. In addition, it may be desirable to sweep with air or some other gas in order to minimize the effects of any hydrogen leakage.

A thermal efficiency, η_t, can be defined for electrolysis cells, analogous to the fuel cell efficiency definition presented in textbooks on fuel cells [Hoogers, 2003; Laramie and Dicks, 2000; EG&G Tech. Serv., 2002]. The thermal efficiency quantifies the heating value of the hydrogen produced by electrolysis per unit of electrical energy consumed in the stack. Based on this definition,

$$\eta_t = \frac{\Delta H_R \dot{N}_{H2}}{VI} \tag{4}$$

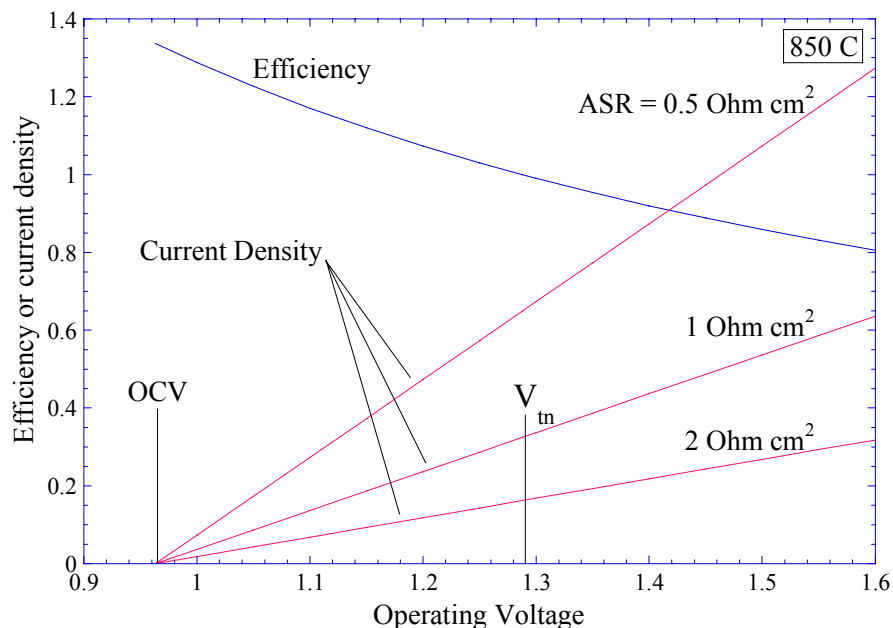Eliminating the current I, the thermal efficiency can be expressed in terms of cell operating potential

Figure 7. Effect of operating voltage and area-specific resistance on electrolysis efficiency.

as:

$$\eta_t = \frac{\Delta H_R / 2F}{V} = \frac{V_{tn}}{V} .$$ (5)

The thermal efficiency for the fuel-cell mode of operation is the inverse of Eqn. (5).

It should be noted that the value of the thermal efficiency defined in this manner for electrolysis can exceed 1.0. As an example, for the reversible stoichiometric case, the cell potential approaches reference open-cell value, $E_o = \Delta G_R / 2F$, yielding:

$$\eta_{t,max} = \frac{\Delta H_R}{\Delta G_R}$$ (6)

which for steam electrolysis at 850°C is equal to 1.34. For cases with variable gas concentrations, the open-cell potential is given by the Nernst Equation, which for the hydrogen/oxygen/steam system takes the form:

$$E = E_o - \frac{RT}{jF} \ln\left[\left(\frac{y_{H2O}}{y_{H2} y_{O2}^{1/2}} \right) \left(\frac{P}{P_{std}} \right)^{-1/2} \right]$$ (7)

The corresponding efficiency limit varies accordingly. It is not desirable to operate an electrolysis stack near this efficiency limit, however, because the only way to approach this limit is to operate with very low current densities. There is a trade-off between efficiency and hydrogen production rate in selecting an electrolysis stack operating voltage. This trade-off is illustrated in Figure 7. The upper curve in the figure shows the decrease in electrolysis efficiency that occurs as the per-cell operating voltage is increased above the open-cell voltage (OCV). At the thermal-neutral voltage, the electrolysis efficiency is 1.0. The bottom curves show the effect of operating voltage and area-specific resistance (ASR) on the current density. If a target current density (and corresponding hydrogen production rate) is selected, lower ASR values allow for stack operation at lower voltages and higher efficiencies.
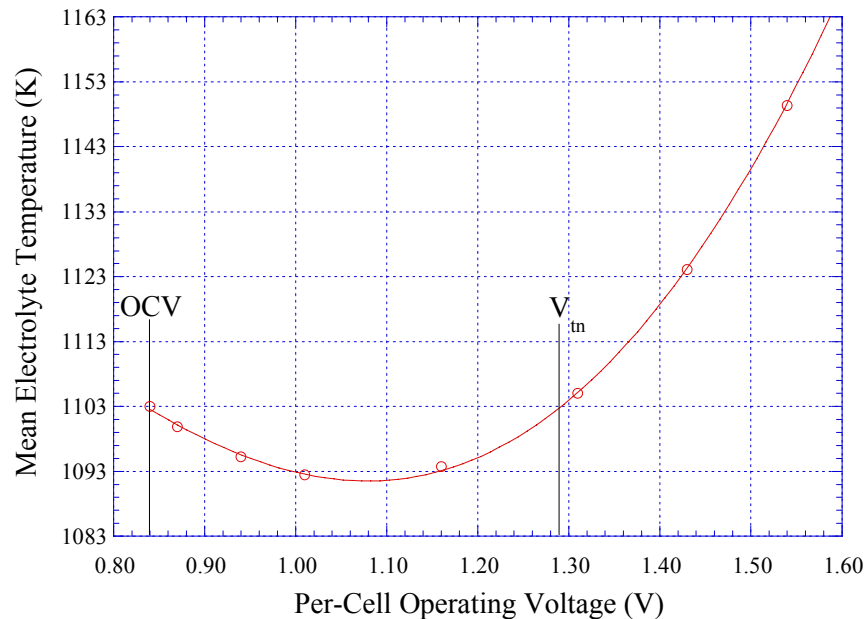

Figure 8. Mean electrolyte temperature versus operating voltage for the base case.
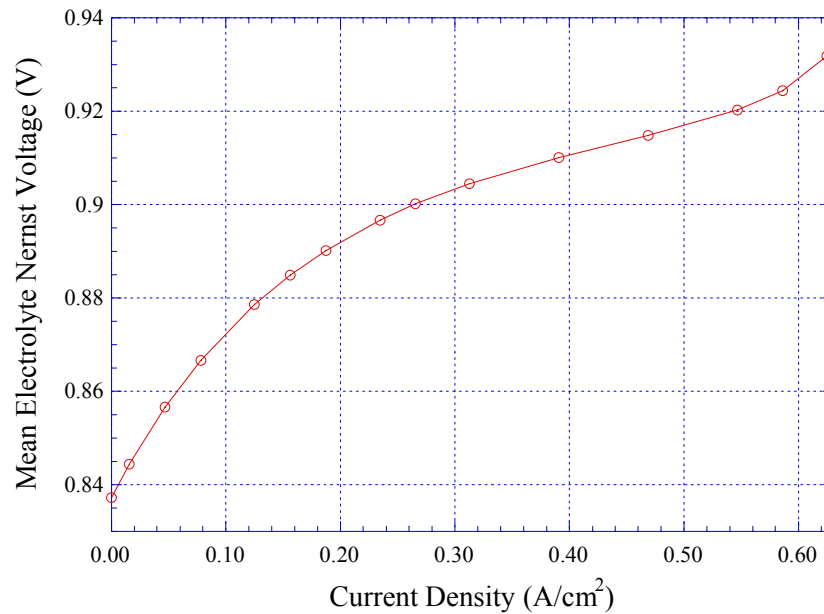
Figure 9. Mean Nernst potential versus current density for base case.

4. RESULTS

Results of the FLUENT simulations obtained for various cases are presented in Figures 8 through 16. Figure 8 shows the predicted mean electrolyte temperature as a function of operating voltage for the base case. Electrolyte temperatures at each operating voltage are determined by the interplay of five mechanisms: (1) convection heat transfer with gas inlet temperatures set at 1103 K (830ºC), (2) heat conduction through the electrolyte and surrounding materials, (3) radiation heat transfer from the edge of the model to an oven temperature set at 1103 K, (4) endothermic heat of reaction requirement associated with the electrolysis process, and (5) ohmic heating from the electronic and ionic resistances in the electrolyte, gap resistances, and other materials. The thermal neutral voltage, V_{tn}, for steam electrolysis at 830ºC is 1.287 V, as indicated on the figure. At this operating voltage, the endothermic reaction heat requirement and the ohmic heat generation are balanced and the mean electrolyte temperature is essentially the same as the gas inlet and radiant temperatures. The solid line in Figure 8 represents a 4th-order polynomial curve fit to the predicted electrolyte temperatures. At operating voltages between the open-cell potential and thermal neutral, electrolyte temperatures are below 1103 K. A thermal minimum temperature occurs near an operating voltage of 1.08 V. For operating voltages above thermal neutral, ohmic heating dominates and resultant electrolyte temperatures rapidly increase beyond 1103 K. This thermal behavior has been verified through recent experimental measurements of internal stack temperatures (O'Brien et al., 2005) obtained from an operating stack using miniature thermocouples.

The mean Nernst potential across the electrolyte is shown in Fig. 9 as a function of current density. At zero current density (a current of 10^{-6} A was specified in the FLUENT model), the Nernst potential corresponds to the open-cell potential predicted from Eqn. (7) using a stack temperature of 1103 K and the specified gas inlet compositions. Of course, at zero current density, there is no change in gas composition as the gases flow through the stack, so the Nernst potential is uniform across the electrolyte. However, for nonzero current densities, in the electrolysis mode, the mole fraction of steam decreases across the stack, the mole fraction of hydrogen increases across the stack, and, on the air side, the mole fraction of oxygen increases in the cross-flow direction. The mean Nernst potential is also affected by the electrolyte temperature corresponding to each operating point, but this effect is small. The net result is that the mean Nernst potential increases with increasing operating voltage and
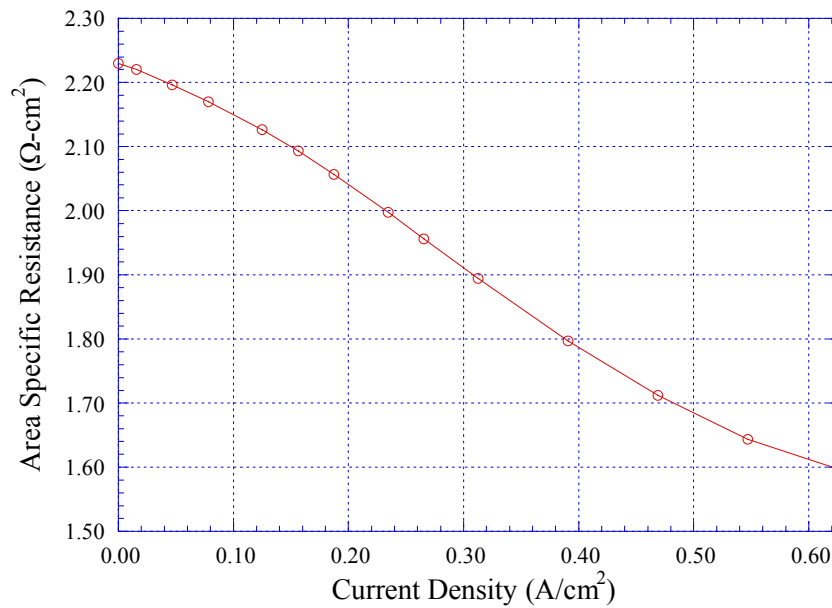
Figure 10. Per-cell area-specific resistance versus current density.

current density. In general the shape of this curve is dominated by the logarithmic term in the Nernst Potential equation.

Mean per-cell area-specific resistance (ASR) is presented in Fig. 10 for the operating model cell as a function of current density. ASR values are calculated as the difference between the operating voltage and the open-cell potential divided by the current density. ASR values decrease with increasing current density, consistent with the concave-down V-i curves shown in Fig. 5 for both the FLUENT predictions and the experimental data.

Mean outlet mole fractions of steam, hydrogen, and oxygen are presented in Fig. 11 as a function of current density. Since there is a direct linear proportionality between stack electrical current and steam consumption/hydrogen production (Faraday's law), and since every mole of steam consumed results in one mole of hydrogen produced (i.e., the total number of moles of gas on the
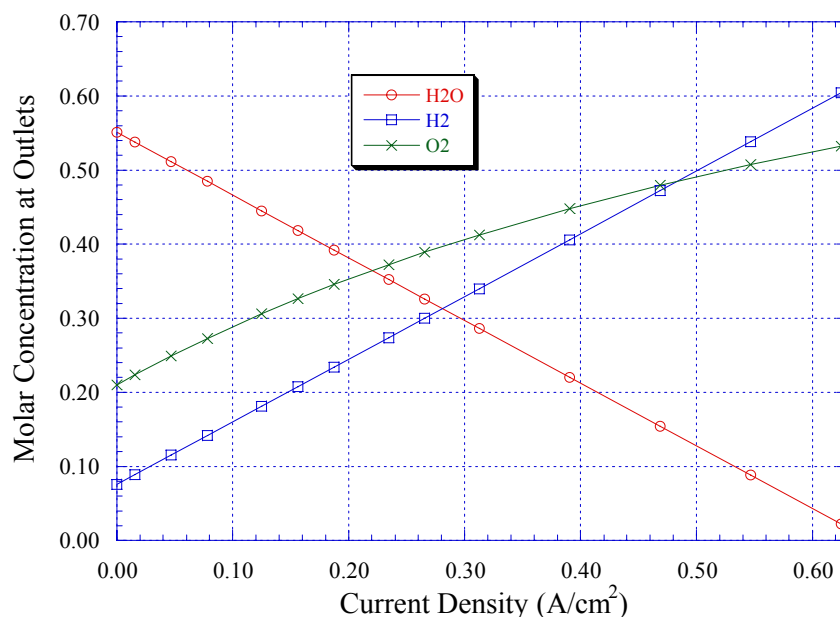

Figure 11. Mean molar fractions of steam, hydrogen, and oxygen at stack outlet versus current density for base case.

steam/hydrogen side is constant), the outlet hydrogen and steam mole fractions vary linearly with current density. Furthermore, the sum of the mole fraction of hydrogen plus the mole fraction of steam is a constant (0.623 in this particular case). Note that the outlet steam mole fraction at the highest current density is very close to zero. At this current density, the outlet end of the cell is nearly at steam starvation. On the air side, oxygen is evolved as a result of the electrolysis process. Since the total number of moles of air increases as oxygen is evolved, the oxygen mole fraction increases nonlinearly with current density.

A series of plots showing the effects of perturbations from the base case on the cell i-V curves and electrolytes temperatures is presented in Figs. 12 (a)-(d).   Each figure shows the i-V and temperature curves for the base case plus two perturbation curves. The temperature values refer to the left-side vertical axis and the voltage values refer to the right-side vertical axis. Fig. 12 (a) shows the effect of increasing the gas inlet and radiant temperatures by ±50 K. Electrolyte temperatures show similar trends as the base case, incremented by ±50 K. The i-V curve for the +50 K case has a shallower slope, corresponding to a lower ASR due to the increased ionic conductivity of the electrolyte at that elevated temperature. Fig. 12 (b) shows the effect of increasing or decreasing the steam content of the inlet gas flow. The perturbation cases are for twice the baseline steam flow (2.0 x H2O) and half the baseline steam flow (0.5 x H2O). The i-V curve for the reduced steam flow case ends a little past 0.3 A/cm^2 current density due to steam starvation. The FLUENT SOFC module cannot reach a converged solution in this case. The effects of the different steam flow rates on the electrolyte temperature are small. Fig. 12 (c) shows the effects of varying the total gas flow rate by a factor of one-half (0.5 x flow) or a factor of ten (10 x flow). The 10 x flow case shows a much flatter temperature profile due to the much larger heat capacity rates of the gases flowing through the cell. The i-V curve for the 10 x flow case is more linear than the base case, due to the flatter composition
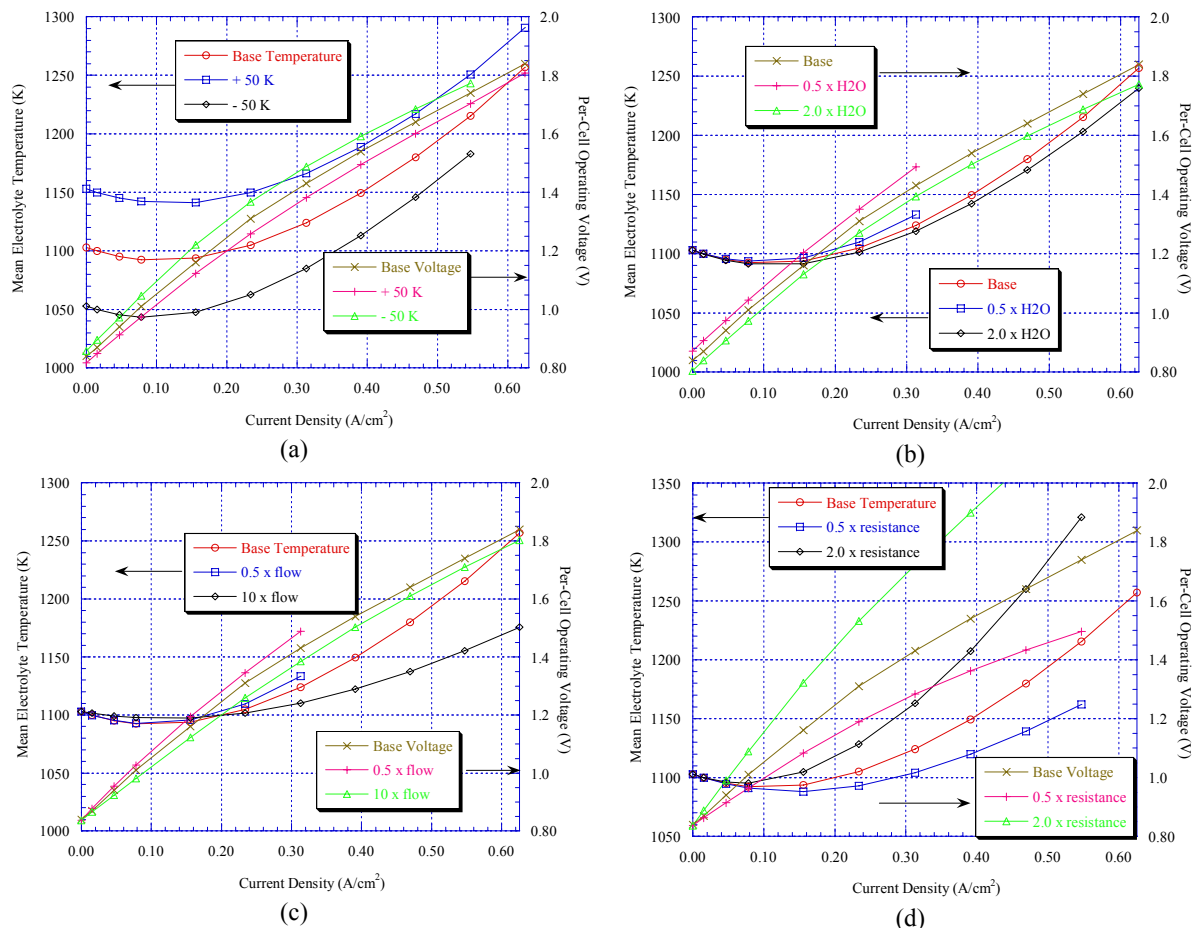

Figure 12. Mean electrolyte temperature and cell operating voltage versus current density for various perturbations from the base case; (a) inlet gas temperature at ±50 K, (b) water mass concentration at 0.5 and 2.0 times base case, (c) flow rates on steam and oxygen side at 0.5 and 10 times base case, (d) resistance between flow channel and electrode at 0.5 and 2.0 times base case.

and temperature profiles associated with the higher flow rate. Once again, steam starvation occurs for the 0.5 x flow case at a current density just above 0.3 A/cm^2. Fig. 12 (d) shows the effect of varying the gap resistances between the electrodes and the flow fields by a factor of one-half (0.5 x resistance) or two (2 x resistance). Electrolyte temperatures and cell i-V behavior are very sensitive to the gap resistance values used in the model. The 2.0 x resistance case shows much higher electrolyte temperatures and voltage values at a given current density. Similarly, the 0.5 x resistance case shows much lower electrolyte temperatures and voltages.

A series of contour plots representing local FLUENT results for temperature, current density, Nernst potential and hydrogen mole fraction is presented in Figs. 13-16. In these figures, the steam/hydrogen flow is from top to bottom and the air flow is from left to right. Figure 13 shows electrolyte temperature contour plots for amperages of 10, 15, and 30 amps. These current values correspond to operating voltage regions shown on Figure 8 near the minimum electrolyte temperature (10 amps), near thermal neutral voltage (15 amps), and in the region dominated by ohmic heating (30 amps). The radiant boundary condition at 1103 K tends to hold the outside of the model at a higher temperature for the 10-amp case (Fig. 13 (a))while the endothermic heat requirement maintains the center of the electrolyte at a lower temperature. Minimum and maximum temperatures for this case are 1091 K and 1100 K respectively. The center Fig. 13 (b) shows a temperature difference across the electrolyte of only one degree K, with values very near 1103 K; this current density is very near the thermal neutral voltage. Fig. 13 (c) shows that ohmic heating in the electrolyte is dominating and the thermal boundary condition is keeping the edges cooler than the inside. Minimum and maximum temperatures are 1139 K and 1197 K, respectively, for this case.

Contour plots of local current density on the electrolyte are shown in Figure 14 for 10, 15, and 30 amps. Mean current densities for these three cases are: 0.156, 0.234, and 0.469 A/cm^2. These plots correlate directly with local hydrogen production rates. Since FLUENT is being run in electrolysis mode, the current density values are all negative and hence the blue values have the largest magnitudes. Highest current density magnitudes occur near the steam hydrogen inlet (the top of the figures). This corresponds to the location of the greatest steam concentration. The orange areas show where the current density is lowest because the available steam concentration is lower.

Figure 15 shows the local variation in Nernst potential for currents of 10, 15, and 30 amps. The minimum Nernst voltage occurs at the top left of the plots where the steam and oxygen concentrations are the highest and hydrogen concentration the lowest. The minimum value for the Nernst voltage in these three plots is 0.84 V, while the maximum increases from 0.91 V to 0.93 V to 0.99 V as the
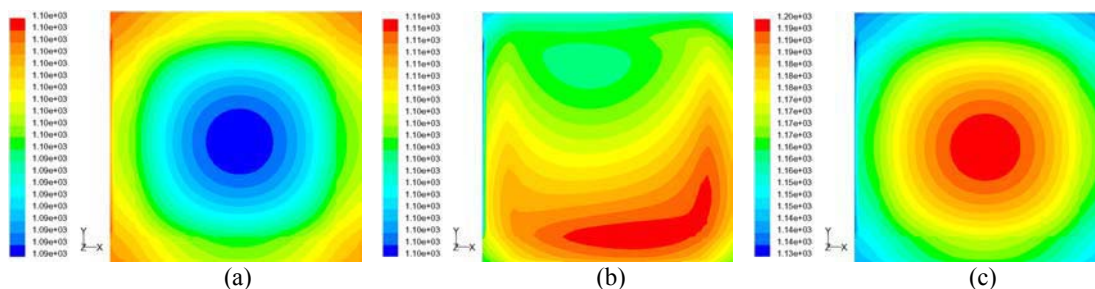

| (a) | (b) | (c) |

Figure 13. Temperature (K) contours on the electrolyte and insulator for currents of 10, 15, and 30 amps.

| (a) | (b) | (c) |

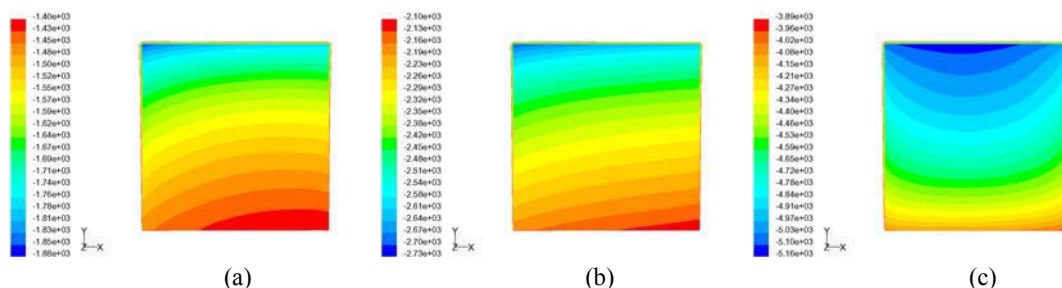**Figure 14.** Current density (A/m^2) contours on the electrolyte for currents of 10, 15, and 30 amps.

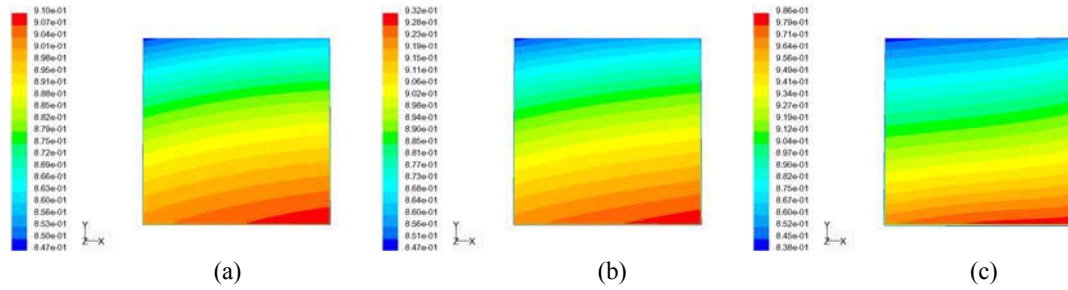(a)   (b)   (c)

Figure 15. Nernst potential (V) contours on the electrolyte for currents of 10, 15, and 30 amps.

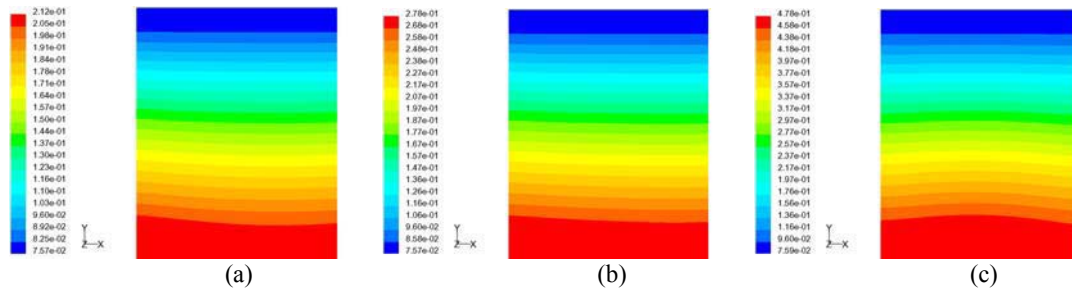(a)   (b)   (c)

Figure 16. Contours of hydrogen mole fraction in hydrogen flow channel for currents of 10, 15, and 30 amps.

current increases from 10 to 30 amps respectively. Maximum Nernst voltage occurs in the bottom right where the steam concentration is the lowest. The highest Nernst potential regions correspond to the lowest current density regions. Note that the variation in Nernst potential indicated in these plots is dominated by gas concentration effects, rather than thermal effects.

Molar hydrogen fraction contours are shown in Figure 16 for currents of 10, 15, and 30 amps. These contours show the entire steam/hydrogen flow channel, including the top and bottom regions adjacent to the edge rails where no hydrogen production is occurring. Hydrogen concentration increases as the flow progresses through the channel from top to bottom. There is a slight bump of higher concentration at the left side of the flow channel for the first two plots and in the center for the third plot. This corresponds to the local variation in current densities. As shown in Figures 11 and 16, the hydrogen concentration at the outlet is 0.21, 0.28, and 0.48 for the three cases.

5.   CONCLUSIONS

A three-dimensional computational fluid dynamics (CFD) model has been created to model high-temperature steam electrolysis in a planar solid oxide electrolysis cell (SOEC). The model represents a single cell as it would exist in an electrolysis stack. Details of the model geometry are specific to a stack that was fabricated by Ceramatec, Inc. and tested at the Idaho National Laboratory. Mass, momentum, energy, and species conservation and transport are provided via the core features of the commercial CFD code FLUENT. A solid-oxide fuel cell (SOFC) model adds the electrochemical reactions and loss mechanisms and computation of the electric field throughout the cell. The FLUENT SOFC user-defined subroutine was modified for this work to allow for operation in the SOEC mode. Model results provide detailed profiles of temperature, Nernst potential, operating potential, anode-side gas composition, cathode-side gas composition, current density and hydrogen production over a range of stack operating conditions. Mean model results are shown to compare favorably with experimental results obtained from an actual ten-cell stack tested at INL. At operating voltages between the open-cell potential and thermal neutral, electrolyte temperatures are below 1103 K. A thermal minimum temperature occurs near 1.08 V. For operating voltages above thermal neutral, ohmic heating dominates and resultant electrolyte temperatures rapidly increase beyond 1103 K. This thermal behavior has been verified through recent experimental measurements of internal stack temperatures (O'Brien et al., 2005) obtained from an operating stack using miniature

thermocouples. Mean Nernst potentials increases with increasing operating voltage and current density. The rate of increase in Nernst potential is high at low current densities, moderate at intermediate current densities, and high again at high current densities where steam starvation begins to occur. Mean per-cell ASR values decrease with increasing current density, consistent with experimental data. Predicted mean outlet hydrogen and steam concentrations vary linearly with current density, as expected. Effects of variations in operating temperature, gas flow rate, and contact resistance from the base case were presented. Contour plots of local electrolyte temperature, current density, and Nernst potential indicated the effects of heat transfer, reaction cooling/heating, and change in local gas composition.

NOMENCLATURE

ASR area specific resistance, Ω-cm^2
E voltage potential, V
F Faraday constant, 96487 J/V-mol
ΔG Gibbs free energy, J/mol
ΔH molar enthalpy of reaction, J/mol
I current, A
j electrons transferred per H2 molecule
K permeability, m^2
k thermal conductivity, W/m^2-K
$\dot{N}$ molar flow rate, mol/s
P pressure in stack, Pa
Q external heat transfer, W
R universal gas constant, J/mol-K
T temperature, K
W work, product of I*V, W
y molar fraction

Greek Letters

φ porosity
σ electrical conductivity Ω^{-1}m^{-1}
η efficiency

Subscripts

$H2$ Hydrogen gas
$H2O$ steam
o open-cell
$O2$ Oxygen
R reaction
std standard pressure
tn thermal neutral
t thermal

ACKNOWLEDGEMENTS

REFERENCES

EG&G Technical Services, Science Applications International Corporation, *Fuel Cell Handbook*, 6th Ed., DOE/NETL 2002/1179, 2002.

FLUENT Theory Manual, version 6.1.22, Fluent Inc., Lebanon, New Hampshire, 2004.

Herring, J. S., O'Brien, J. E., Stoots, C. M., Lessing, P. A., Anderson, R. P., Hartvigsen, J. J., and Elangovan, S., "Hydrogen Production from Nuclear Energy via High-Temperature Electrolysis," presented at the 2004 International Conference on Advances in Nuclear Power Plants (ICAPP '04), June 13-17, 2004, Pittsburgh, PA.

Herring, J. S., O'Brien, J. E., Stoots, C. M., Lessing, P. A., Anderson, R. P., Hartvigsen, J. J., and Elangovan, S., "Hydrogen Production through High-Temperature Electrolysis Using Nuclear Power," presented at the AIChE Spring National Meeting, New Orleans, April 25 – 29, 2004.

Hoogers, G. (ed.), *Fuel Cell Technology Handbook,* CRC Press, New York, 2003.

International Atomic Energy Agency (IAEA), May 1999, *Hydrogen as an energy carrier and its production by nuclear power*, IAEA-TECDOC-1085.

National Academy of Sciences, National Research Council, *The Hydrogen Economy: Opportunities, Costs, Barriers, and R&D Needs*, February, 2004.

O'Brien, J. E., Stoots, C. M., Herring, J. S., and Lessing, P. A., "Characterization of Solid-Oxide Electrolysis Cells for Hydrogen Production via High-Temperature Steam Electrolysis," Proceedings, 2nd International Conference on Fuel Cell Science, Engineering, and Technology, June 14-16, 2004, Rochester, NY, paper# 2474, pp., 219 – 228.

O'Brien, J. E., Stoots, C. M., Herring, J. S., and Lessing, P. A., "Performance Measurements of Solid-Oxide Electrolysis Cells for Hydrogen Production from Nuclear Energy," Proceedings, 12th ICONE Meeting, April 25-29, 2004, Arlington, VA, paper # ICONE12-49479.

O'Brien, J. E., Stoots, C. M., Herring, J. S., and Hartvigsen, J. J., "High-Temperature Electrolysis for Hydrogen Production from Nuclear Energy," NURETH-11 Conference, October 2-6, 2005, Avignon, France.

Prinkey, M., Shahnam, M., and Rogers, W. A., "SOFC FLUENT Model Theory Guide and User Manual," Release Version 1.0, FLUENT, Inc., 2004.

Yildiz, B., and Kazimi, M. S., "Nuclear Energy Options for Hydrogen and Hydrogen-Based Liquid Fuels Production," MIT-NES-TR-001, September 2003.